Impact of Surface Chemistry on Nanoparticle-Electrode Interactions in the Electrochemical Detection of Nanoparticle Collisions

Chang-Hui Chen,[a] Emma R. Ravenhill,[a] Dmitry Momotenko,[a] Yang-Rae Kim,[a] Stanley C. S. Lai,[a,b] and Patrick R. Unwin[a,*]

[a] Department of Chemistry, University of Warwick, Gibbet Hill Rd, Coventry CV4 7AL, UK.

[b] MESA+ Institute for Nanotechnology, University of Twente, PO Box 217, 7500 AE Enschede, The Netherlands

[*] To whom correspondence should be addressed: P.R.Unwin@warwick.ac.uk

Abstract

The electrochemical detection of a single nanoparticle (NP) at a support electrode can provide key information on surface chemistry and fundamental electron transfer (ET) properties at the nanoscale. This study employs scanning electrochemical cell microscopy (SECCM) as a fluidic device to both deliver and study the interactions between individual citrate-capped gold nanoparticles (AuNPs) and a range of alkanethiol-modified Au electrodes with different terminal groups, namely, -COOH, -OH and -CH_3. Single NP collisions were detected by the AuNP-mediated ET reaction to $Fe(CN)_6^{4-/3-}$ in aqueous solution. The collision frequency, residence time and current-time characteristics of AuNPs is greatly affected by the terminal groups of the alkanethiol. Methods to determine these parameters, including the effect of the instrument response function, and derive ET kinetics are outlined. To further understand the interactions of AuNPs with these surfaces, atomic force microscopy (AFM) force measurements were performed using citrate-modified Au-coated AFM tips and the same alkanethiol-modified Au substrates in aqueous solution at the same potential bias as for the AuNP collision experiments. Force curves on OH-terminated surfaces showed no repulsion and negligible adhesion force. In contrast, a clear repulsion (on approach) was seen for COOH- terminated surface and adhesion forces (on retract) were observed for both COOH- and CH_3-terminated surfaces. These interactions help to explain the residence times and collision frequencies in AuNP collisions. More generally, as the interfacial properties probed by AFM appear to be amplified in NP collision experiments, and new features also become evident, it is suggested that such experiments provide a new means of probing surface chemistry at the nanoscale.

Introduction

Metal nanoparticles (NPs) find many applications in numerous fundamental and applied fields, with electrochemical studies particularly prominent.[1-2] The electrochemical activity of a NP not only depends on the intrinsic electron transfer (ET) properties of the NP, but also on the interaction between the NP and the support electrode surface.[3-4] While tremendous efforts have been made to understand correlations between NP properties and NP electroactivity,[5] interactions between NPs and electrode surfaces have been studied much less.

To investigate the interaction between a NP and an (electrode) surface, well-defined and thoroughly characterized model systems are needed. Self-assembled monolayers (SAMs), particularly alkanethiol monolayers on gold electrodes, which we use herein, are useful in this respect, as they form well-defined films with the possibility of a high degree of control over the thickness (within ~ 1 Å, one CH_2 group), and a wide range of accessible terminal group chemical functionalities.[6-7] The ET probability across an insulating layer, such as a SAM, separating an electrode and a redox species in solution is proportional to $\exp(-\beta d)$, where d is the thickness of the insulating monolayer and β is the tunneling decay constant (β ~ 1 $Å^{-1}$ for a saturated hydrocarbon chain).[8] Consequently, SAMs with carbon chains longer than 10 carbon atoms (~ 1 nm) are expected to effectively block ET between a species in solution and the electrode surface, with little faradaic current flow. Interestingly, the Fermín[9-10] and Gooding[11] groups found that electron tunneling from redox species to electrodes could be restored by NP adsorption on top of the insulating layer. This phenomenon was further interpreted by a theoretical framework proposed by Chazalviel and Allongue.[12] The basis of this model is that electronic coupling between a NP and a support electrode may be sufficiently strong to allow the NP to facilitate ET between the support electrode and solution redox species. While this model has been validated for NP-mediated ET on a macroscopic

scale, much less is known about a single NP in this configuration.

To electrochemically detect single NPs, the main approaches rely on separating the responses of individual NPs, either spatially and/or temporally.[5] For the latter, Bard's group introduced a novel strategy by performing NP-impact experiments on bare ultramicroelectrodes (UMEs).[13-15] In this approach, a conductive support electrode is held at a potential at which it is kinetically inert towards an (electrocatalytic) reaction of interest. As a single NP in solution collides with the electrode, the contact sets up a reaction at the NP, giving rise to a change in the faradaic current. Since its introduction, this methodology has been employed by several research groups to study different combinations of electrode materials and redox mediators.[16-21] Two general types of signals, staircase or blip, have been reported so far in these NP-impact experiments. Staircase signals are found in systems where particles sequentially adhere to the electrode and continuously catalyze the reaction, so that with each NP addition, the current-time curve is a series of current jumps (new NP arrived) and plateaus.[22-24] Blip responses are produced when NPs only interact with electrodes for a short amount of time.[25]

Besides using bare UMEs, there are a few recent reports of using chemically-modified UMEs to perform NP-impact experiments.[3, 26-27] For example, Bard's group[26] recently performed Pt NP collisions at a Pt UME passivated with a thin TiO_2 film, in solutions containing $K_3Fe(CN)_6$, and rationalized their findings in a recent model taking mass transport of the redox species, electron transfer kinetics at the NP surface and electron tunneling through the insulating layer into account.[28] The TiO_2 film blocked the conductive Pt UME surface but allowed electron tunneling through the film when Pt NPs landed on the surface, in (qualitative) agreement with the Chazalviel-Allongue model described above.[12] The Crooks' group[27] studied Pt NP collisions at an Au UME modified with polyelectrolyte multilayer films (up to 5 nm thick) for the electrooxidation of N_2H_4. For Pt NPs with a diameter of ~ 57

nm, there was sufficient electronic coupling through the films for electrocatalysis to occur upon Pt NP collision with the UME. Pt NP collision frequencies were controlled by manipulating the electrostatic charge presented by the polyelectrolyte multilayer films.

In this paper, we investigate the effect of the surface functionality of the collector (support) electrode on NP interactions by using scanning electrochemical cell microscopy (SECCM). This technique has several advantages over NP-impact experiments with UMEs. First, due to the small size of the pipet (ranging from 1.5 to 3.0 μm), which is used to form an electrochemical cell with a substrate (electrode) of interest by meniscus contact, the background current is significantly decreased. Second, electrode materials which cannot be fabricated as UMEs can be used as the collector electrode in SECCM.[29] Third, one can select an area of interest on a substrate to carry out measurements, a feature we use herein to identify areas with very high quality SAM organization (low background current). Fourth, although not exploited in this work, one can easily use an electric field to control the delivery of particles and for particle counting.[30] The principles of this technique for NP detection are shown in Figure 1. A meniscus at the end of a double barrel pipet forms a small electrochemical cell with an alkanethiol modified Au (SAM/Au) substrate that is used as the electrode. This electrode is inert towards ferrocyanide ($Fe(CN)_6^{4-}$) oxidation, and in the absence of AuNPs, there is essentially no interfacial electron transfer. However, AuNP collisions on the surface form an AuNP/SAM/Au structure and electron transfer between $Fe(CN)_6^{4-}$ and the Au substrate (mediated by the AuNP) occurs.

These interactions were further investigated by performing AFM force measurements, using a citrate-coated AFM tip and substrates modified by SAMs with the same terminal group functionalities (-OH, -COOH and $-CH_3$). We discuss these interactions in terms of surface wetting, hydrogen bonding and surface charge, and assess their implications for NP-impact experiments. Our aim is to provide new insights into the nature of NP-substrate

interactions and their impact on ET processes. A further outcome of the work is that NP collisions provide a sensitive means of probing surface chemistry.

Experimental Section

Chemicals. Potassium ferrocyanide trihydrate (≥ 98.5 %; Sigma-Aldrich), potassium chloride (≥ 98 %; Sigma-Aldrich), dichlorodimethylsilane (≥ 99 %; Acros Organics), ethanol absolute (analytical reagent; VWR Chemicals), 11-mercapto-1-undecanol (97 %; Sigma-Aldrich), 11-mercaptoundecanoic acid (95 %; Sigma-Aldrich), dodecanethiol (≥ 97 %; Sigma-Aldrich) and AuNP stock solution (10 nM, stabilized suspension in 0.4 mM citrate buffer; Sigma-Aldrich) were used as received. All aqueous solutions were prepared from high purity water (SELECT-HP, Purite, 18.2 MΩ cm resistivity at 25 °C).

Preparation of Au and SAM/Au electrodes. Au electrodes were prepared on silicon oxide/silicon wafers (n-type, 525 μm thick, IDB Technologies Ltd, UK) using an electronic thermal beam evaporator (Moorfield MiniLab 080 platform) under high vacuum ($\leq 1 \times 10^{-6}$ mbar) to deposit a 40.0 nm Au film on top of a 2.0 nm Cr adhesion layer. Three different types of alkanethiols were employed to form SAMs, with different terminal groups, namely two hydrophilic groups (11-mercapto-1-undecanol, (HS-$(CH_2)_{11}$-OH, hereafter denoted OH_{SAM}) and 11-mercaptoundecanoic acid (HS-$(CH_2)_{10}$-COOH, hereafter $COOH_{SAM}$)) and one with a hydrophobic terminal group (dodecanethiol (HS-$(CH_2)_{11}$-CH_3, hereafter $CH_{3,SAM}$)). The SAMs were formed by immersing the Au electrodes into an ethanol solution containing 2 mM of the alkanethiol of interest for at least 24 hrs. Then, they were rinsed with copious amounts of ethanol to remove any excess alkanethiol and dried under nitrogen flow. All functionalized electrodes were used immediately after preparation to minimize contamination from air. Before performing NP-impact experiments, electrochemical measurements using cyclic voltammetry (CV, see below and Supporting Information, Figure

S-1) were performed on the SAM/Au electrodes to check the monolayer quality.

Pipet fabrication. The pipets used in SECCM were pulled from borosilicate theta capillaries (TG 150-10, Harvard Part No. 30-0114) using a Sutter P-2000 laser puller (Sutter Instruments, USA). These pipets were silanized in dichlorodimethylsilane under argon gas flowing through, to increase the hydrophobicity of the outer walls. Pipet sizes, ranging from 1.5 ~ 3.0 μm diameter were measured accurately using a Zeiss SUPRA 55 variable-pressure field emission-scanning electron microscope **(**FE-SEM**)**.

Macroscopic cyclic voltammetry (CV). Macroscopic CVs at bare Au and SAM/Au electrodes were recorded in a conventional three-electrode system using a CH Instruments (CHI-730a) potentiostat, in which Au or SAM/Au working electrodes were covered with droplets (*ca.* 3 μL) containing 1 mM $K_4Fe(CN)_6$ and 100 mM KCl. An AgCl-coated Ag wire (Ag/AgCl/(100 mM KCl)) and a Pt wire were used as a reference and a counter electrode, respectively. No attempt was made to precisely measure the working electrode area, which depended on the wetting of the SAM substrate.

SECCM measurements. NP-impact experiments were carried out using the SECCM-based setup shown in Figure 1. A double barrel pipet was mounted on a high-dynamic *z*-piezoelectric positioner (P-753.3CD LISA, PhysikInstrumente), while the working electrode (Au or SAM/Au substrate) was mounted on a high-precision *x*,*y*-piezoelectric stage (P-622.1CL or P-622.2CL PIHera, PhysikInstrumente). Ag/AgCl wires were inserted into each barrel of the pipet to serve as quasi-reference counter electrodes (QRCEs). Before and after CV or chronoamperometric measurements, a bias potential, V_2, was applied to the QRCEs to check the resistance of electrolyte, which is a good indicator of droplet size.[31-32] No bias potential was applied during the measurements. Rather, both QRCEs were held at a potential of V_1 relative to ground. The working electrode was also held at ground, and thus had an effective potential, $-V_1$, with respect to the QRCEs.

For SECCM chronoamperometric measurements, the pipet slowly approached the substrate at a speed of 100 nm s^{-1}. Meniscus contact resulted in the formation of an electrochemical cell with the substrate, as evidenced by a spike current at the substrate due to double layer charging. The meniscus thickness as estimated from the conductance current was a few hundred nm.[32] This signaled the pipet movement to stop. The potential was then switched to a potential of interest and current-time traces were recorded continuously, using a highly sensitive home-built autoranging current amplifier. The bandwidth of the current amplifier was set to 100 Hz, for the current range used, 10 fA/V to 10 pA/V. The measured signal was passed through a low pass filter at 1 kHz. Data points were collected every 650 μs, with each point being the average of 65 readings, i.e. with a reading acquired every 10 μs, using a field-programmable gate array card (PCI-7830R, National Instruments). All signals that were higher than 2 times the standard deviation of the background were counted automatically as a peak and, after this process, all the peaks found in this way were checked manually.

Herein, all potentials are reported with respect to an Ag/AgCl/(100 mM KCl) reference electrode in the case of macroscopic CVs and an Ag/AgCl QRCE for SECCM studies.

AFM force measurements. All force measurements were performed with a Bruker-Nano Multimode 8 AFM controlled by Nanoscope electronics, utilizing a small flow cell (Bruker). AFM tips were purchased from Bruker (SNL-10) with triangular, silicon nitride cantilevers of 205 μm length. These tips were prepared by depositing a 2.5 nm Cr adhesion layer followed by a 60 nm gold layer using a thermal beam evaporator, giving tips with 60 nm radius of curvature. The adsorption of citrate ions on these tips was carried out using a literature procedure[33] by immersing the gold coated AFM tips in 1 mM sodium citrate solution for at least 12 hrs.

All the AFM force curves were recorded under potential-control in a two-electrode system using a CH Instruments potentiostat. The SAM/Au substrate of interest was the working electrode and an Ag/AgCl wire (50 μm in diameter) placed in the inlet channel of the cell, served as a QRCE. All measurements were performed in an aqueous solution containing 1 mM $K_4Fe(CN)_6$ and 0.4 mM sodium citrate, to ensure the ionic strength was the same as that in NP-impact experiments. During AFM measurements, a constant potential of 400 mV was applied to the working electrode. The background currents at these potentials were negligible, justifying the use of a two-electrode system and QRCE.

The spring constant of each tip used was measured using the thermal tune method integrated into the Nanoscope software, with a mean value of 0.118 ± 0.010 nN nm^{-1} for the tips used. Raw data were converted to obtain force *vs*. piezo displacement plots, using the measured deflection sensitivities and tip spring constants. For each substrate, more than 200 force-distance curve measurements were performed at multiple substrate areas.

Results and discussion

Electrochemical characterization of substrates (collector electrodes)

Typical CVs (scan rate 100 mV s^{-1}) for the oxidation of 1 mM $K_4Fe(CN)_6$ in 100 mM KCl at a microscopic gold electrode with and without the different SAMs are given in Supporting Information (Figure S-1). The voltammetric response at a bare Au electrode shows the expected reversible redox behavior, with a peak-to-peak separation of ~ 60 mV, characteristic of a facile outer-sphere redox mediator such as $Fe(CN)_6^{4-/3-}$ on a metal electrode surface. Modification of the electrode by an alkanethiol SAM strongly inhibits the electrochemical reaction, as evident from the much decreased current magnitudes in Figure S-1, indicative of well-ordered closely packed SAMs.[9, 34] Upon closer inspection, it can also be observed that the extent to which the SAM inhibits ET depends, to some degree, on the

terminal groups. The electrochemical activity decreases in the order of OH_{SAM}/Au > $CH_{3,SAM}$/Au > $COOH_{SAM}$/Au, which is determined by the electrostatic forces associated with the terminal groups and the (negatively-charged) redox species.[35] Nonetheless, irrespective of the end-termination, the blocking of ET by all the SAMs is sufficient for these electrodes to be regarded as electrochemically 'inert' for the NP-impact experiments that follow.

To further verify the quality of SAMs at the microscopic scale, as well as to validate our approach, micro-scale CVs of Au and SAM/Au electrodes were recorded using the SECCM setup, with a pipet of ~ 3 μm diameter, with some results shown in Figure 2. Clearly, all of the SECCM CVs of SAM/Au electrodes showed considerable blocking towards $Fe(CN)_6^{4-}$ oxidation. The extremely low current response of the SAM/Au electrode indicates that the SECCM setup is close to ideal for the proposed studies. It is important to note that pinholes can be present in the SAMs (as inferred from the macro-CVs discussed above). This could also be seen sometimes with SECCM, with CVs produced that had a relatively high current (Supporting Information, Figure S-1b). However, a key feature of our technique is that we can use the surface current as an indicator of local SAM quality, by landing the pipet on different areas of the substrate and performing chronoamperometric measurements. In this way, we were able to select a 'low background' current area (indicative of a closely-packed SAM layer) to carry out NP-impact experiments. Based on the CVs, all NP-impact experiments were performed at a collector electrode potential of 400 mV, a potential well in the mass transport-limited regime for $Fe(CN)_6^{4-}$ oxidation at both macroscopic Au surface and SECCM configuration on the CV timescale, but as we will show below, where kinetics effects have to be considered (and can be revealed) for $Fe(CN)_6^{4-}$ oxidation at AuNPs, due to the much higher mass transport rates at isolated NPs.

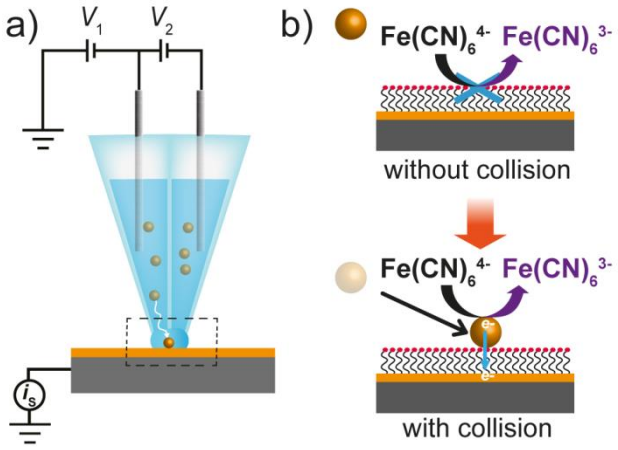

Figure 1 a) Schematic of the SECCM setup. V_1 is the potential at which SECCM conductive cell is floated with respect to ground and V_2 is the bias potential between the QRCEs in the pipet. The current flowing through the working electrode is denoted by i_s. b) Principle of the electrochemical detection of a single AuNP collision on an alkanethiol modified substrate. Top: an alkanethiol monolayer effectively inhibits electron transfer between a redox species ($Fe(CN)_6^{4-}$) in solution and an electrode surface. Bottom: an AuNP collision opens up a new electronic pathway and mediates electron transfer.

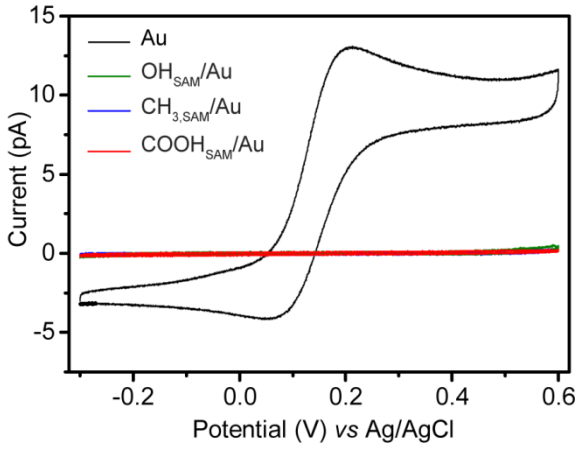

Figure 2 Microscale CVs recorded for bare Au (black line) and various SAM/Au electrodes (colored lines) by using a pipet of 3 μm diameter in the SECCM setup. Electrolyte solution: 1 mM $K_4Fe(CN)_6$ and 20 mM KCl. Scan rate: 100 mV s^{-1}.

NP-impact experiments at SAM/Au electrodes

NP-impact experiments were performed using the SECCM setup with electrolyte solutions containing 1 mM $K_4Fe(CN)_6$ and 5 nM citrate-stabilized AuNPs, with no additional

supporting electrolyte. The average size of the AuNPs was determined by transmission electron microscopy (TEM) and they were found to be 5 nm in radius (Supporting Information, Figure S-2). The stability of the AuNPs in the presence of 1 mM $K_4Fe(CN)_6$ was confirmed by dynamic light scattering measurement (DLS, Supporting Information, Figure S-3). The AuNP concentration chosen ensured that sufficient collision events could be observed and the relatively low ionic strength served to minimize AuNP agglomeration. For all the SAM/Au electrodes, control experiments were performed using pipets of the same size as those used in the collision experiments, with solution containing only 1 mM $K_4Fe(CN)_6$ (*i.e.* no AuNPs). These 'blank' current-time traces are provided in the Supporting Information (Figure S-4). As seen in these traces, after stepping the working electrode potential from -200 mV to +400 mV (as for the NP-impact experiment), there is a charging current, which quickly decays to a current of negligible magnitude, making this a very attractive platform for detecting NP collisions.

AuNP collisions at OH_{SAM}/Au electrodes

A typical current-time trace over a time range of 5 s for AuNP collisions at an OH_{SAM}/Au substrate with a 3 μm diameter pipet is shown in Figure 3a. The current-time trace in the absence of AuNPs in the pipet (Supporting Information, Figure S-4a) is featureless and the longtime current value is small (~ 0.1 pA), indicating negligible electron transfer between $Fe(CN)_6^{4-}$ and the Au electrode. In the presence of AuNPs in the pipet, clear distinctive current peaks in the time-trace are observed, indicating the occurrence of discrete electrochemical reactions on the substrate, due to AuNP collisions. To obtain a detailed view of the transients for each NP collision, we zoom into a small region of the data in Figure 3a (inside the red box), over a time range of ~ 1 s, and plot the data in Figure 3b. This shows that the current spikes are discrete signals, with some variation in the peak current values.

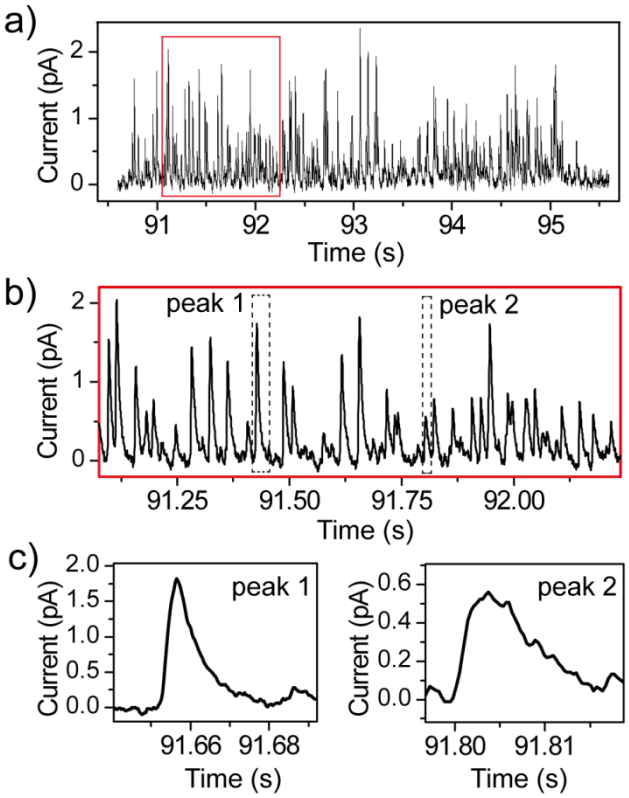

Figure 3. a) Current-time trace for AuNP collisions at an OH_{SAM}/Au electrode bias at 400 mV using a 3 μm diameter pipet. Electrolyte solution: 1 mM $K_4Fe(CN)_6$ and 5 nM AuNP. b) Zoom-in of the current trace within a time range of ~1 s. c) Expanded view of the current transients for peak 1 (high peak current) and peak 2 (low peak current).

Two examples of current-time responses with different peak currents are shown in Figure 3c. Clearly, they both have a relatively fast rise time (within a few ms) to the peak, followed by a slower decay down to the baseline level. Current spikes for NP collisions have been reported extensively,[16, 22] but not with this clarity. In general terms, three distinct mechanisms have been proposed which can yield a spike-shaped transient. First, spikes can be caused by 'elastic' NP collisions.[13, 25] Here, a NP comes into contact (*i.e.* within electron tunneling distance) with the substrate electrode for a brief period of time, before diffusing away. Second, the NPs can be deactivated, either due to 'poisoning' of the reaction by products or intermediates of the probe redox system, or poisoning by the substrate electrode material.[36-37] Finally, the probe redox process can be self-limiting, such as in the case of NP

dissolution or underpotential deposition on the NP.[20, 38]

The redox species used in this work, $Fe(CN)_6^{4-/3-}$, is not expected to cause AuNP poisoning. There are several examples of NPs on SAMs showing high electrochemical activity to support this idea.[9, 39-40] Thus, we can reasonably rule out NP poisoning and self-limiting reactions as causes for the spike shape, and attribute this to a 'semi-elastic' collision of AuNPs on the surface. As the AuNP comes into contact with the SAM/Au electrode, electron tunneling takes place, setting off the redox reaction and giving rise to a rapid increase in electrochemical current. The NP can become trapped (transiently) in the tunneling region or stabilized on the surface for a certain time. Once the NP leaves the tunneling region, the current starts to decay with time.[41]

To obtain more information on these AuNP collisions, statistical analysis was carried out using the data in Figure 3a. The results are summarized in Figure 4a-c, which shows the peak current, NP residence time on the electrode and charge of each collision event, respectively, along with the AuNP size distribution. Further analysis is given in Table 1 and we explain those data in more detail below. The AuNP collision frequency (f) at an OH_{SAM}/Au electrode was determined to be 12.8 $\times 10^4$ s^{-1} pM^{-1} cm^{-2} (Table 1), which is in roughly the same range as reported by other groups (typically ~ 10^4 s^{-1} pM^{-1} cm^{-2}).[5] Collision frequencies are often estimated based on the diffusion-limited flux,[22, 42] although it is important to point out that this assumes that each NP only undergoes a single pass with an electrode, and in fact multiple passes could occur. The estimated theoretical AuNP collision frequency based on a single pass of AuNPs, in this configuration, is *ca.* 25 $\times 10^4$ s^{-1} pM^{-1} cm^{-2} (Supporting Information, SI-4).

The experimental peak current (i_p) distribution (Figure 4a), shows a broad range of values from 0.25 pA to 2.5 pA with a median value of 0.55 pA. An indication of the current expected from a NP collision can be estimated by calculating the steady-state diffusion-

limited current generated at an individual spherical NP in contact with a planar electrode using equation 1,[13-14]

$$i_{\text{lim}} = 4\pi(\ln 2)\text{n}FDcr_{\text{NP}} \quad (1)$$

where n is the number of electrons transferred (1), F is the Faraday constant (96485 C mol^{-1}), D is the diffusion coefficient of $Fe(CN)_6^{4-}$ (6.67×10^{-6} cm^2 s^{-1}),[43] c is the concentration of $Fe(CN)_6^{4-}$ (1 mM), and r_{NP} is the radius of AuNP (5 nm). From equation 1, i_{lim} is 2.8 pA. It can be seen that the overwhelming majority of the responses are smaller than this value. We consider this difference in terms of heterogeneous ET kinetics below.

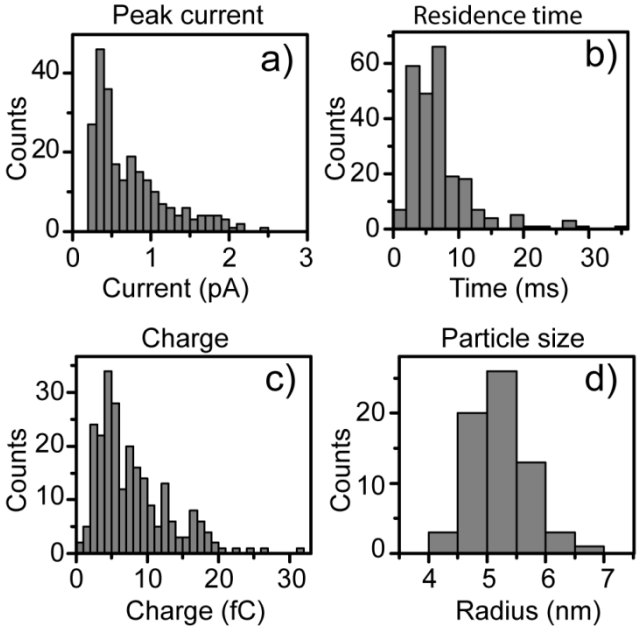

Figure 4. Statistical distributions of a) peak current, b) residence time, and c) charge of AuNP collisions at an OH_{SAM}/Au substrate from the current-time trace in Figure. 3a. d) AuNP particle size distribution, analyzed from TEM images (Supporting Information, Figure S-2).

Table 1. AuNP collision frequencies and the median values of peak current, residence time and charge at three different SAM/Au electrodes. Potential: +400 mV *vs.* Ag/AgCl QRCE.

Electrode	shape	f	i_p	$i_{p,c}$	τ_p	Q
		10^4 s^{-1} pM^{-1} cm^{-2}	pA	pA	ms	fC

OH_{SAM}/Au	spike	12.80	0.55	0.77	6.2	6.30
$COOH_{SAM}$/Au	spike/plateau	4.30	0.47	0.49	17.6	10.03
$CH_{3,SAM}$/Au	spike	0.16	0.21	0.37	7.0	2.00

f, collision frequency; i_p, peak current; $i_{p,c}$, corrected peak current (see text); τ_p, residence time; *Q*, charge. All values of i_p, $i_{p,c}$ τ_p, and *Q* in the Table are median values.

A discussion of the observed residence time is now warranted. For these studies, in order to probe the small currents arising from NP collisions (often < 1 pA), a high sensitivity (charge sensitive) current amplifier was employed with a bandwidth of 100 Hz (corresponding to a ~ 20 ms response time). Importantly, this is orders of magnitude slower than the diffusional timescale of freely diffusing NPs ($\tau_D = L^2/D$, where L is the diffusion length and D the diffusion constant). Considering that the NP needs to remain within tunneling distance (a few nanometers at most) of the electrode surface, and the diffusion coefficient of the NP employed is *ca.* 4.9×10^{-7} cm^2 s^{-1} (Supporting Information, SI-4), τ_D is *ca.* tens of ns. Thus, in order to detect a NP in these studies, the NP must stay near the electrode for a reasonable period of time (several ms and longer) and our measurement recorded such events.

On this timescale, we can consider a NP collision as a binary event (the NP is either in contact or 'far' away from the electrode surface). This would result in an ideal 'on-off' signal as illustrated by the square wave signal in Figure 5. This consideration allows the deconvolution of the current events into a component related to the response of the electronics and a component related to the 'real' occupancy of the NP. The impulse response of the electronics can be written as $(2\pi/\tau)\cdot exp(-2\pi t/\tau)$,[44] where τ is the time constant of current amplifier and t is the time of an event (in this case, residence time of the particle at the support electrode surface). The convolution of these two responses leads to transient signals, in which the instrument effect can be fully taken into account.

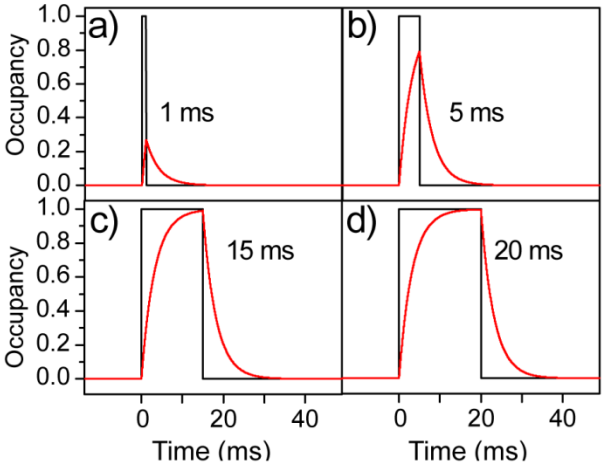

Figure 5. Plots of the occupancy as a function of time (black line) and its convolution (red line) with the electronic impulse function for event time, *t*, values of a) 1 ms, b) 5 ms, c) 15 ms and d) 20 ms.

Using $\tau = 20$ ms, as employed for the studies herein, we calculated the convolution of 'ideal' (binary 'on-off') signals with the impulse response of the electronics for events of different time scales, *t*, ranging from 1 ms to 20 ms, and shown in Figure 5a-d. These figures illustrate a few intuitively simple, but important effects. First, the response time of the electronics leads to a signal with a different shape than the real (square-wave) occupancy signal. In particular, the sharp increase (and decrease) of the square-wave signal are drawn out to a slow rise (and decay) time. Second, the observed signal requires 20 ms to reach the plateau of the real occupancy signal. Consequently, for events shorter than 20 ms, the observed (convoluted) peak value is only a fraction of the 'real' (deconvoluted) value. For events with *t* values ranging from 1 ms to 5 ms, this fraction is between 27 % and 80 %. For *t* > 15 ms, > 99 % of the real occupancy magnitude is recovered. Third, and significantly, the residence time of a NP on the surface is given by the time between the start of the observed signal increase until the start of the decrease of the signal (and not by the total width of the signal). On this basis, residence times for the OH_{SAM}/Au system are summarized in Figure 4b.

For AuNP collision at the OH_{SAM}/Au electrode, the median time is 6.0 ms,

corresponding to an occupancy of 85 %, which means the observed current in the experiments is attenuated to about 85 % of the 'real' value had the measurement electronics responded fully. This partially explains the lower current observed, but is not the main factor for the lower than diffusion-limited values, as discussed below. Importantly, because the occupancy for each signal can be determined, corrected peak currents ($i_{p,c}$), representing what would be the non-attenuated response, can be obtained and they are shown in Table 1. For the OH_{SAM}/Au system, the corrected median current peak value is 0.77 pA.

It is important to point out that as the measurements are made using a charge-sensitive detector, the total charge of an event is conserved. By integrating each current time trace, the total charge (Q) for each collision can further be obtained, as shown in Figure 4c. In this case, the median charge of 6.3 fC corresponds to an event of just 3.7×10^4 electrons. It is important to point out that to equilibrate the potential of the NP in solution with the support electrode upon contact, a charge of up to a few hundred of electrons (~ 10^{-17} C) would be required,[45] which is negligible compared to the charge observed (10^{-15} C). Therefore the observed current cannot be attributed to NP charging alone, and must be almost entirely the result of the redox reaction at the NP surface.

AuNP collisions at $COOH_{SAM}$ /Au electrodes

To gain further insight into the effect of the surface functionality on NP electrocatalytic impacts, we employed 11-mercaptoundecanoic acid ($COOH_{SAM}$), which provides a different hydrophilic surface. Figure 6a shows a typical current-time trace for AuNP collisions on a $COOH_{SAM}$/Au, using a 1.5 μm diameter pipet. Due to the low collision frequency of this substrate, partly due to the use of a smaller pipet, data were collected and analyzed over a longer time period compared that for OH_{SAM} substrate. Again, a control experiment showed a featureless background (Supporting Information, Figure S-4b). A

zoomed-in current-time trace in Figure 6b gives a clearer view of distinctive collision signals. In contrast to AuNP collisions at an OH_{SAM}/Au electrode (above), AuNP collisions at $COOH_{SAM}$/Au electrodes can be separated into two distinct types of signals, as marked by '°' and '*' in Figure 6b and 6c. The first type of signal, marked by '°', consists of spike, with the current rising to peak value and then decaying, similar to the signal observed for AuNP collisions at the OH_{SAM}/Au electrode. In contract, the second type of signal (marked by '*') shows a current plateau of a few tens of milliseconds. These two different signal traces suggest two distinct types of interactions of AuNPs with the substrate, which we will discuss in detail later.

Similar to the analysis for OH_{SAM}/Au electrodes, histograms of peak current, residence time, and charge are shown in Supporting Information (Figure S-5a) and summarized in Table 1. The frequency of AuNP collisions on $COOH_{SAM}$/Au electrodes, *ca.* 4.3×10^4 s^{-1} pM^{-1} cm^{-2} (Table 1), is approximately three times smaller than that for the OH_{SAM}/Au (12.8×10^4 s^{-1} pM^{-1} cm^{-2}). We attribute this decrease in collision frequency to the electrostatic repulsion between the (partially) negatively charged surface due to deprotonated carboxylate groups at the pH of the measurement,[46-47] *ca.*7.3, and the negatively charged colloidal AuNPs (from the stabilizing citrate). Such effects have been reported previously to explain the low collision frequency of Pt NPs at a 3-mercaptopropionic acid modified Au UME for hydrazine oxidation.[22]

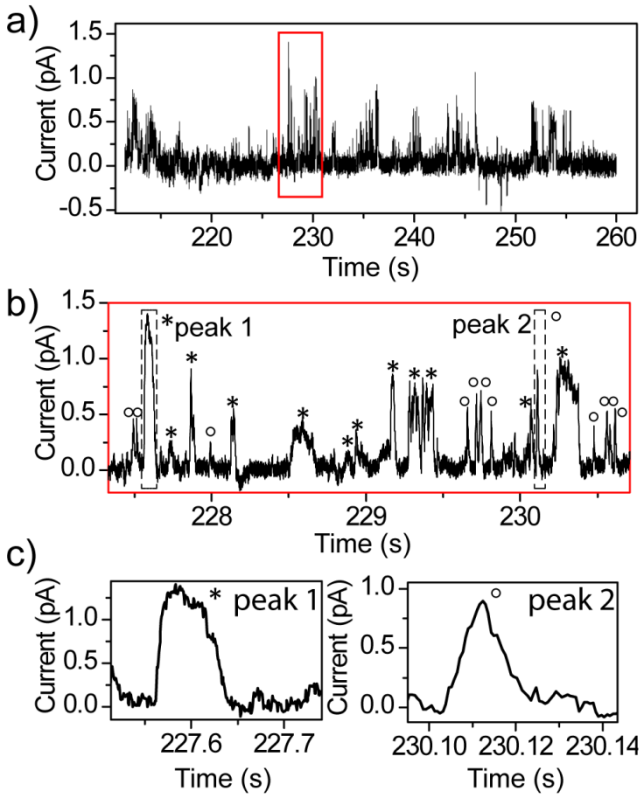

Figure 6. a) Current-time trace for AuNP collisions at a $COOH_{SAM}$/Au substrate using a 1.5 μm diameter pipet. b) Zoom-in of current transients within a time range of ~3.0 s. The transients display two types of peaks. Peaks displaying a plateau current are marked with '*', while sharp spikes are marked with '°' c) Typical current transients of a plateau peak (peak 1, '*') and a spike peak (peak2, '°').

The median residence time for AuNPs on a $COOH_{SAM}$/Au is longer than for an OH_{SAM}/Au (17.6 ms *vs.* 6.2 ms) substrate. As a consequence, by deconvoluting the measured signal from the instrumental response, as described above for OH_{SAM}/Au, we found that the majority of the peak current magnitudes (> 90 %) were within 90 % of the real, deconvoluted signal. The corrected median peak current value was found to be 0.49 pA (Table 1), essentially the same as the raw data, 0.47 pA. This indicates that most of the NP collisions detected at this substrate are long enough for the current amplifier to detect a fully amplified signal. A notable result from these studies is that the median current at this substrate is similar to that for the OH_{SAM}/Au substrate, indicating that ET at the AuNPs is essentially

independent of the surface termination groups for the two hydrophilic substrates.

AuNP collisions at $CH_{3,SAM}$/Au electrodes

Finally, to explore a wide range of surface chemistry, we employed hydrophobic dodecanethiol-modified Au electrodes. Figure 7a shows a typical current-time trace recorded for AuNP impacts on a $CH_{3,SAM}$/Au electrode with a pipet of 3.0 μm diameter. Again, distinctive current spikes can be observed compared to the background current (Supporting Information, Figure S-4c). Figure 7b is an expanded view of the current transients over a time range of 2 s. Figure 7c shows two typical current-time transients with different peak current magnitudes. Similar to AuNP collisions at the OH_{SAM} covered surfaces, all the collisions were found to give 'spike' type signals.

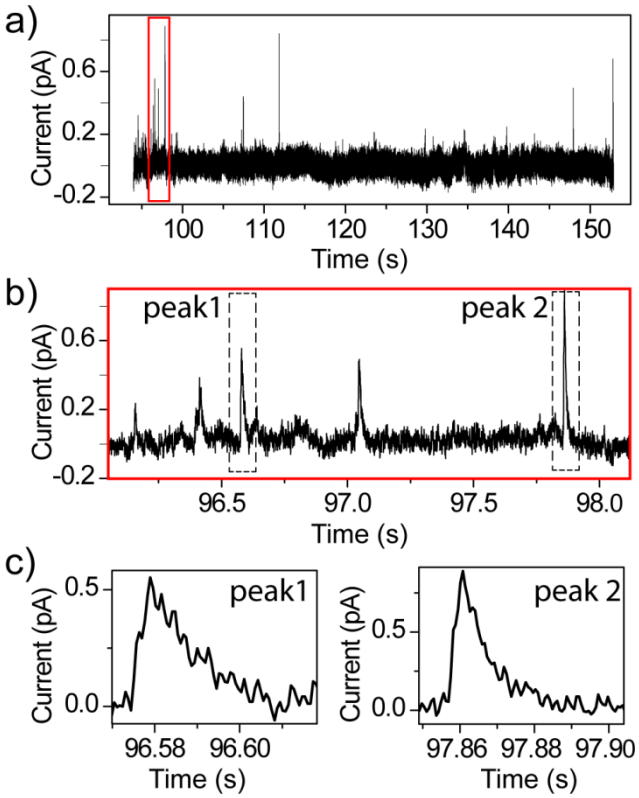

Figure 7. a) Current-time trace of AuNP collisions at $CH_{3,SAM}$/Au electrode. b) Zoom-in of current events within a time range of 2 s. c) Typical current transients of events with a low (peak 1) and a high (peak 2) peak current value.

Similar to the above two systems, an analysis of peak current, residence time, peak charge and collision frequency can be found in Supporting Information (Figure S-5b), with a summary of the data provided in Table 1. The collision frequency on $CH_{3,SAM}$/Au was found to be 0.16 s^{-1} pM^{-1} cm^{-2}, approximately one order of magnitude smaller than the values obtained for the hydrophilic surfaces. The median residence time for AuNP collisions at this electrode was 7.0 ms, similar to that for an OH_{SAM}/Au, while the raw median peak current was 0.21 pA and the value after correction for the instrument response function was 0.37 pA. This latter value is a little lower than that for the two hydrophilic substrates (see above and Table 1).

Kinetics analysis

To gain more insights into the kinetics of the electron transfer through SAMs, a finite element method model was developed to calculate the steady state current for the $Fe(CN)_6^{4-}$ oxidation process at a AuNP on a film at the potential of the electrode as a function of the standard heterogeneous ET rate constant, k^0 (Butler-Volmer kinetics). The details of modeling and results are outlined in Supporting Information (SI-6). A working curve (Figure S-7) of current *vs*. $\log(k^0)$ was calculated from the simulations, from which k^0 values could be extracted from the experimental data. We consider the median values for this analysis, which represent the characteristic behavior of the NPs. The corrected median $i_{p,c}$ for OH_{SAM}/Au, $COOH_{SAM}$/Au and $CH_{3,SAM}$/Au electrodes, are 0.77, 0.49 and 0.37 pA (Table 1), corresponding to apparent rate constant values, k^0, of 15.3×10^{-3}, 8.5×10^{-3} and 6.1×10^{-3} cm s^{-1} respectively. The k^0 values obtained herein are consistent with k^0 values reported in the literature for NP mediated electron transfer to $Fe(CN)_6^{4-/3-}$ across insulating layers,[10] and are also reasonably in line with the rate constant reported for this couple at polycrystalline Au electrodes.[10, 48-49] Although there is a trend in the rate constants, the values are reasonably

close and it is difficult to make definitive statements as to the origin of any differences in apparent electron transfer kinetics between the systems. We would, however, point out that, for the conditions of these measurements, where the Debye length (~ 3 nm) is of the order of the diffusion layer around the NP (~ 5 nm radius), nanoscale surface charge and double layer effects will be important[50-56] for both the kinetics and the mass transport. These effects will be sensitive to the local environment of AuNPs on the different SAMs. In particular, the partially negatively charged groups from the $COOH_{SAM}$ may lead to a local decrease in $Fe(CN)_6^{4-}$ concentration as well as inhibit mass transport, which is seen in kinetics (lower current), when comparing the data for OH_{SAM}/Au and $COOH_{SAM}$/Au. The water and double layer structure at the $CH_{3,SAM}$ (for hydrophobic surfaces generally)[57] will be very different to that at the hydrophilic SAMs, which again will impact mass transport and apparent kinetics (currents). We pick up some of these issues in the next section.

AFM force measurements

To obtain further in-depth understanding of AuNP-substrate interactions, we performed AFM force measurements, which can be highly revealing of the interaction forces between an AFM tip and a substrate of interest.[58-59] Herein, gold coated-AFM tips were used that had radii of curvature of ~ 60 nm, and were modified with citrate (see experimental section) to serve as a model for citrate-capped AuNPs. Force-distance curves were recorded in several areas on all three SAM/Au substrates, to determine whether there was any inhomogeneity in the surface functionalization.

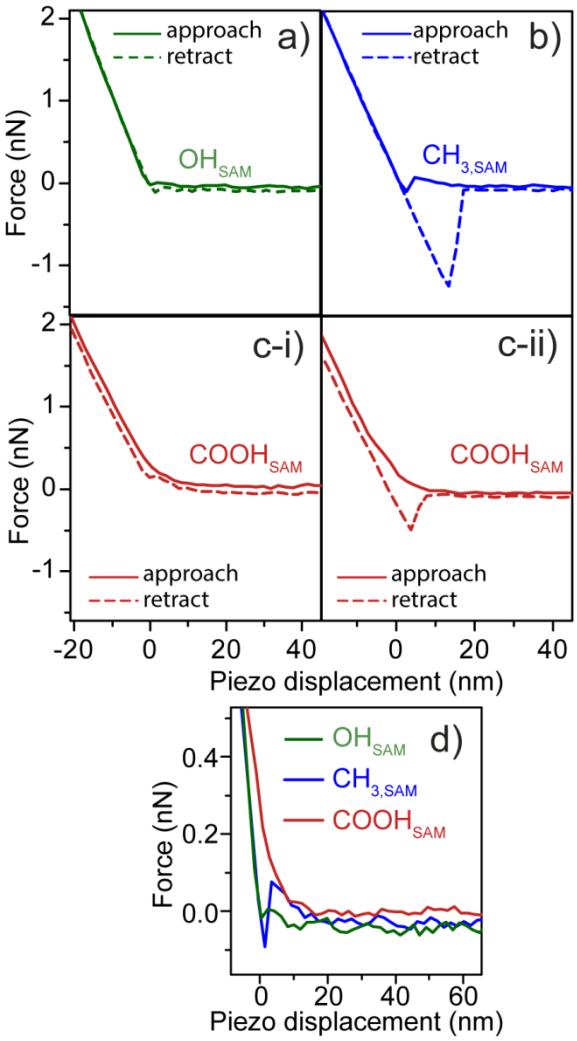

Figure 8. a-d) Representative force-piezo displacement curves (in aqueous solution containing 1 mM $K_4Fe(CN)_6$ and 0.4 mM sodium citrate) obtained for citrate-modified AFM tips with substrates modified by three different alkanethiols: a) OH-terminated; b) CH_3-terminated; and c-i) COOH-terminated first curve, c-ii) COOH-terminated second curve. d) Comparison of the approach curves for the three different substrates. The origin corresponds to the initial contact between the tip and the substrate, as determined by the onset of the linear regime of each approach curve. Measurements were made under electrochemical control, with each of the substrates bias at 400 mV *vs.* Ag/AgCl QRCE.

Figures 8a-c shows typical force-distance curves (here as force *vs.* displacement of the piezoelectric actuator) obtained on the three SAM/Au substrates (see caption and experimental section for details). Three characteristic regions can be distinguished in these

force-displacement curves. At large distances (the 'zero-region'), there is no effective interaction between the tip and the substrate, and the force is zero. Upon moving the tip towards the surface (decreasing the piezo-displacement), the forces start to deviate from zero ('interacting region'). After the tip physically contacts the surface (at zero displacement), a linear force-displacement relation is observed with a slope equal to the spring constant of the cantilever, typical for hard (*i.e.* non-deformable) contact (the 'contact region').[59]

We will discuss the two hydrophilic substrates first. For the OH_{SAM}/Au (Figure 8a), the zero-region is directly followed by the contact region, and no interaction (attractive or repulsive) during approach or adhesion during retraction of the tip is observed. In comparison, for the $COOH_{SAM}$/Au (Figures 8c-i and 8c-ii), a weak but clear repulsive force was observed at short distances (< 10 nm), as can be seen from the non-linear deviation of the force-distance curve from the zero-force baseline. We attribute this to the electrostatic repulsion between the partially negatively charged carboxylate groups at the substrate and on the tip, as the solution used had a bulk pH ~ 7.3, while typical pK_a for surface-confined COOH groups range from 5.5-10.3,[46-47, 60] with complete deprotonation ranging from pH 7-10 depending on the ionic strength. In addition to the solution pH, the surface acid/base properties of the SAMs can be controlled by the electrode potential.[61-62] The short-range nature of this interaction is in agreement with the Debye screening length in this solution (~3 nm).[63] We believe this repulsion can reasonably be correlated with the lower NP collision frequency on $COOH_{SAM}$ (relative to OH_{SAM}), as a colloidal AuNP needs to come within electron tunneling distance of the electrode surface to be detected electrochemically. In further support of our arguments, we note that earlier cavity-ring down spectroscopy studies of similar citrate-protected AuNPs on clean (negatively charged) glass surfaces found no evidence of long-term accumulation of AuNPs.[64]

On the retraction of the tip, two types of curves are observed for the $COOH_{SAM}$. The

first type (Figure 8c-i) is essentially the reverse of the approach curve. The second type (Figure 8c-ii) shows an apparent adhesion (with a maximum adhesion force of ~ 0.68 ± 0.23 nN, Supporting Information, Figure S-8b) between the tip and the substrate. This adhesion can be attributed to some hydrogen bonding between the citrate COOH-groups on the AFM tip and the surface-COOH groups. The heterogeneity in the force curve characteristics implies some variation on the extent of surface protonation/deprotonation across the surface at the nanoscale, in which the potential applied plays a complicated role.[65] Note that due to the pH of the solution (~7.3) used herein, the $COOH_{SAM}$-citrate adhesion force is much lower than the reported value for completely protonated COOH-COOH groups at pH < 5 (7.0 ± 0.2 nN) for a similar tip radius.[58]

Interestingly, for the NP collisions on the $COOH_{SAM}$, two types of electrochemical response were observed (*vide supra*). The existence of two types of signals in the NP impact experiments ('spike' *vs*. 'plateau') and in the force measurements (no adhesion *vs*. adhesion) suggests that there may be a correlation between the NP collision and force curve characteristics. Thus, we hypothesize that the 'spike' signals correspond to case where no adhesion is detectable in the force-distance curve (as these types of signals were the only type observed on the OH_{SAM}), whereas the 'plateau' signals correlate with the stronger adhesion case. For the OH_{SAM}, the NP-surface interaction forces are weak, and as a result of the random movement of the NP, contact is established and broken ('kiss-and-run'), probably many times and with high frequency (compared to the electrochemical measurement response time) so that a continuous signal is seen,[42] before the NP diffuses into bulk solution again. For the $COOH_{SAM}$, there is a small repulsive interaction between the colloidal NP and the surface, so that upon approach to the surface, a NP may be repelled from the electrode, before any detectable electrochemistry is seen, leading to a lowered collision frequency. If the NP overcomes the repulsive barrier and comes into contact with the electrode, there are two

scenarios. Contact is quickly established and broken (as for OH_{SAM}), leading to 'spike' signal. Alternatively, with stronger hydrogen bond formation, the NP is 'trapped' within tunneling distance for a longer period of time, and a plateau signal with a longer residence time is observed. In all cases, the NP will eventually diffuse into the solution, marking the end of the signal. This process may be aided by the electrochemical process: an uneven distribution of the redox reaction rate across the NP surface, may lead to some electrochemical propulsion as seen for large 'swimmer' particles in solution.[41, 66]

Finally, we provide a brief discussion of the hydrophobic surface. A typical force curve for the $CH_{3,SAM}$/Au substrate (Figure 8b) shows a number of features. Upon approach, a small repulsive force (< ~20 nm, comparable to $COOH_{SAM}$, Figure 8) is observed. This is followed by an apparent snap-to-contact at small distances. During the retraction of AFM tips, a significant adhesion was observed, extending over almost 20 nm of piezo displacement with a maximum adhesion force of ~ 1.2 nN. Such force-distance traces have been observed for hydrophobic surfaces in aqueous solutions, and are typically correlated with a hydrophobic interaction.[59] The origin of this hydrophobic interaction is still under debate and a few hypotheses exist, including a change in water structure at interfaces,[67] the electrostatic interactions in water or on the surface[68] and the presence of vapor cavities or surface nanobubbles at hydrophobic surfaces.[59, 69] Surface nanobubbles have been observed with AFM imaging on a number of different hydrophobic surfaces, particularly in non-degassed solutions (such as the air saturated solutions in this research).[70-71] Such nanobubbles, which are either formed spontaneously or due to initial contact of AFM tips, cause strong attractions while also bridging with each other,[72] leading to a long range adhesion force in AFM force curves due to capillarity effects. Importantly, for significantly hydrophobic surfaces (contact angles > 100°), it is found that up to 90 % of a hydrophobic surface may be covered by surface nanobubbles.[71] Such an extensive coverage of the surface with nanobubbles would be

consistent with the studies herein, as we found that all force-distance measurements displayed a similar trace, implying that the interaction between the AFM tip and the nanobubbles is probed (rather than the interaction between the tip and the 'bare' SAM-covered surface). This high coverage implies that in electrochemical measurements, the surface is covered by insulating nanobubbles with patches of the bare electrode surface between the bubbles less than the size of the modified AFM tip (~ 60 nm radius of curvature), resulting in a partially blocked electrode. We believe that this is the main cause of the low AuNP collision frequency on the hydrophobic $CH_{3,SAM}$/Au substrate compared to the two hydrophilic surfaces as only NPs (10 nm diameter; smaller than the AFM tip) colliding with the bare surface will lead to a electrochemical signal, whereas NP collisions on a nanobubble will be separated by a thick insulating layer. In fact, the apparently small proportion of the surface that is bare and the strong adhesion between a citrate-covered gold surface and the nanobubble-covered hydrophobic surface (as evident from Figure 8b) would trap AuNPs at the nanobubble-modified parts of the surface. This would lead to a much lower electrochemical collision frequency, as seen in our experiments. Finally, the short interaction time in these particle collision experiments demonstrates that there is little stabilization between the AuNP and the bare (electrochemically active) substrate, a new finding that we were unable to obtain from the AFM measurements due to the size of the AFM probe. This serves to highlight how electrochemical NP collision experiments can reveal new aspects and features on surface chemistry that are not possible from existing other nano-tools.

Conclusions

In this paper, we have investigated the interaction between single AuNPs and a support electrode with different chemical functionality using an SECCM-based probe technique. SAM-modified Au electrodes with different surface properties serve as 'inert'

electrodes towards an electrochemical reaction with a solution redox-couple, $Fe(CN)_6^{4-}$/ $Fe(CN)_6^{3-}$. The collision of AuNPs opens up a new electrochemical pathway, where electron tunneling can occur between the passivated Au electrode and the AuNPs where the redox reaction occurs. Both the small contact area in SECCM and the insulating SAM film-modified electrode allow us to achieve extremely low background currents, and therefore detect electrochemical responses for a single AuNP across an insulating layer with exquisite sensitivity. The results demonstrate that the substrate properties have a significant influence on AuNP collision behavior. To further understand the behavior, these interactions were studied using AFM force measurements.

The results of both the NP-impact experiments and AFM force measurements give rise to similar conclusions. i) AuNPs interact weakly with OH_{SAM} modified surfaces. This is demonstrated by the lack of adhesion force seen for this substrate from AFM force measurements with a citrate-modified gold tip, and the low residence times in NP-impact experiments. However, the higher collision frequencies seen for this surface can be explained by the lack of repulsion seen in the force measurements. ii) Some repulsion is observed between AuNPs and $COOH_{SAM}$ surfaces during AFM approach curves, with small adhesion forces observed on the retract. This leads to some repulsion in the collision experiments, but if a NP overcomes this and makes contact with the substrate, it is stabilized. The result is lower collision frequencies but higher residence times for this substrate. iii) For hydrophobic surfaces with CH_3 surface groups, the lowest collision frequencies are observed in AuNP-impact experiments, which we tentatively ascribe to the surface having an extensive coverage by nanobubbles, as seen for hydrophobic surfaces in aqueous solution.[70-71]

In general, we have demonstrated the applicability of SECCM-based NP-impact experiments for probing intermolecular interactions, especially if combined with AFM force measurements. Notably, subtle variations in the small interaction forces between a NP and a

support electrode on a molecular level can have significant effects on NP collision behavior and ET properties at individual NPs. In addition, some subtle differences that are manifest in AFM measurements are amplified in electrochemical NP collision parameters, such as collision frequencies and residence times. This suggests that NP collision can be used to probe surface chemistry. At the same time, the AFM and the NP-impact techniques approaches are complementary, as they rely on measuring different physical properties (ET activity *vs*. interacting forces), providing a synergistic approach for exploring NP-substrate intermolecular interactions. Thus, although on the whole, the electrochemical measurements of NP collisions are consistent with AFM force measurements, NP collisions provide a new, alternative method for investigating interfaces and the interactions of NPs with surfaces. Such measurements are of key importance for understanding and developing NP applications in many research fields and technologies.

ACKNOWLEDGMENTS

This project was supported by a European Research Council Advanced Investigator Grant (ERC-2009-AdG 247143 "QUANTIF") to P.R.U. and Marie Curie Intra-European Fellowships within the 7th Framework Program of the European Commision (Project Nos. 275450; "VISELCAT" to S.C.S.L. 626158; "FUNICIS" to D.M.) and a University of Warwick Chancellor's International Scholarship awarded to C.-H.C. Y.-R. Kim was further supported by Basic Science Research Program through the National Research Foundation of Korea (2012R1A6A3A03039226). We thank Dr. Kim McKelvey and Dr. Alex Colburn (University of Warwick) for their expert contributions on SECCM instrumentation and custom electronics. We also thank Dr. Robert Lazenby, Dr. Joshua Byers and David Perry for fruitful discussions and help with some of the data analysis.

ASSOCIATED CONTENTS

Supporting Information

The following information is available:

SI-1. Cyclic voltammetry characterization of bare Au and alkanethiol modified Au electrode

SI-2. Transmission electron microscopy (TEM) and dynamic light scattering (DLS) measurements of gold nanoparticles (AuNPs)

SI-3. Current response for SAM/Au electrodes in the absence of AuNPs

SI-4. Estimation of AuNP collision frequency

SI-5. Statistical analysis for AuNPs collisions at 11-mercaptoundecanoic acid and 1-dodecanethiol substrates

SI-6. Finite element method modeling

SI-7. Histograms of adhesion forces from atomic force microscopy force measurements

This material is available free of charge via the internet at http://pubs.acs.org.

REFERENCES

1. Cox, J. T.; Zhang, B. Nanoelectrodes: Recent Advances and New Directions. *Annu. Rev. Anal. Chem.* **2012,** *5*, 253-272.
2. Hernández-Santos, D.; González-García, M. B.; García, A. C. Metal-Nanoparticles Based Electroanalysis. *Electroanalysis* **2002,** *14*, 1225-1235.
3. Xiao, X.; Pan, S.; Jang, J. S.; Fan, F.-R. F.; Bard, A. J. Single Nanoparticle Electrocatalysis: Effect of Monolayers on Particle and Electrode on Electron Transfer. *J. Phys. Chem. C* **2009,** *113*, 14978-14982.
4. Hayden, B. E. Particle Size and Support Effects in Electrocatalysis. *Acc. Chem. Res.* **2013,** *46*, 1858-1866.
5. Kleijn, S. E. F.; Lai, S. C. S.; Koper, M. T. M.; Unwin, P. R. Electrochemistry of Nanoparticles. *Angew. Chem. Int. Ed.* **2014,** *53*, 3558-3586.
6. Love, J. C.; Estroff, L. A.; Kriebel, J. K.; Nuzzo, R. G.; Whitesides, G. M. Self-Assembled Monolayers of Thiolates on Metals as a Form of Nanotechnology. *Chem. Rev.* **2005,** *105*, 1103-1170.
7. Chidsey, C. E. D.; Loiacono, D. N. Chemical functionality in self-assembled monolayers: structural and electrochemical properties. *Langmuir* **1990,** *6*, 682-691.
8. Adams, D. M.; Brus, L.; Chidsey, C. E. D.; Creager, S.; Creutz, C.; Kagan, C. R.; Kamat, P. V.; Lieberman, M.; Lindsay, S.; Marcus, R. A.; Metzger, R. M.; Michel-Beyerle, M. E.; Miller, J. R.; Newton, M. D.; Rolison, D. R.; Sankey, O.; Schanze, K. S.; Yardley, J.; Zhu, X. Charge Transfer on the Nanoscale: Current Status. *J. Phys. Chem. B* **2003,** *107*, 6668-6697.
9. Zhao, J.; Bradbury, C. R.; Huclova, S.; Potapova, I.; Carrara, M.; Fermín, D. J. Nanoparticle-Mediated Electron Transfer Across Ultrathin Self-Assembled Films. *J. Phys. Chem. B* **2005,** *109*, 22985-22994.
10. Zhao, J.; Bradbury, C. R.; Fermín, D. J. Long-Range Electronic Communication between Metal Nanoparticles and Electrode Surfaces Separated by Polyelectrolyte Multilayer Films. *J. Phys. Chem. C* **2008,** *112*, 6832-6841.
11. Shein, J. B.; Lai, L. M. H.; Eggers, P. K.; Paddon-Row, M. N.; Gooding, J. J. Formation of Efficient Electron Transfer Pathways by Adsorbing Gold Nanoparticles to Self-Assembled Monolayer Modified Electrodes. *Langmuir* **2009,** *25*, 11121-11128.
12. Chazalviel, J.-N.; Allongue, P. On the Origin of the Efficient Nanoparticle Mediated Electron Transfer across a Self-Assembled Monolayer. *J. Am. Chem. Soc.* **2010,** *133*, 762-764.
13. Bard, A. J.; Zhou, H.; Kwon, S. J. Electrochemistry of Single Nanoparticles via Electrocatalytic Amplification. *Isr. J. Chem.* **2010,** *50*, 267-276.

14. Xiao, X.; Bard, A. J. Observing Single Nanoparticle Collisions at an Ultramicroelectrode by Electrocatalytic Amplification. *J. Am. Chem. Soc.* **2007,** *129,* 9610-9612.
15. Tel-Vered, R.; Bard, A. J. Generation and Detection of Single Metal Nanoparticles Using Scanning Electrochemical Microscopy Techniques. *J. Phys. Chem. B* **2006,** *110,* 25279-25287.
16. Dasari, R.; Robinson, D. A.; Stevenson, K. J. Ultrasensitive Electroanalytical Tool for Detecting, Sizing, and Evaluating the Catalytic Activity of Platinum Nanoparticles. *J. Am. Chem. Soc.* **2013,** *135,* 570-573.
17. Fosdick, S. E.; Anderson, M. J.; Nettleton, E. G.; Crooks, R. M. Correlated Electrochemical and Optical Tracking of Discrete Collision Events. *J. Am. Chem. Soc.* **2013,** *135,* 5994-5997.
18. Alligrant, T. M.; Anderson, M. J.; Dasari, R.; Stevenson, K. J.; Crooks, R. M. Single Nanoparticle Collisions at Microfluidic Microband Electrodes: The Effect of Electrode Material and Mass Transfer. *Langmuir* **2014,** *30,* 13462-13469.
19. Guo, Z.; Percival, S. J.; Zhang, B. Chemically Resolved Transient Collision Events of Single Electrocatalytic Nanoparticles. *J. Am. Chem. Soc.* **2014,** *136,* 8879-8882.
20. Pearson, A.; O'Mullane, A. P. Nanoparticle-electrode collisions as a dynamic seeding route for the growth of metallic nanostructures. *Chem. Commun.* **2015,** *51,* 5410-5413.
21. Dasari, R.; Tai, K.; Robinson, D. A.; Stevenson, K. J. Electrochemical Monitoring of Single Nanoparticle Collisions at Mercury-Modified Platinum Ultramicroelectrodes. *ACS Nano* **2014,** *8,* 4539-4546.
22. Xiao, X.; Fan, F.-R. F.; Zhou, J.; Bard, A. J. Current Transients in Single Nanoparticle Collision Events. *J. Am. Chem. Soc.* **2008,** *130,* 16669-16677.
23. Kleijn, S. E. F.; Serrano-Bou, B.; Yanson, A. I.; Koper, M. T. M. Influence of Hydrazine-Induced Aggregation on the Electrochemical Detection of Platinum Nanoparticles. *Langmuir* **2013,** *29,* 2054-2064.
24. Jung, A. R.; Lee, S.; Joo, J. W.; Shin, C.; Bae, H.; Moon, S. G.; Kwon, S. J. Potential-Controlled Current Responses from Staircase to Blip in Single Pt Nanoparticle Collisions on a Ni Ultramicroelectrode. *J. Am. Chem. Soc.* **2015,** *137,* 1762-1765.
25. Zhou, H.; Fan, F.-R. F.; Bard, A. J. Observation of Discrete Au Nanoparticle Collisions by Electrocatalytic Amplification Using Pt Ultramicroelectrode Surface Modification. *J. Phys. Chem. Lett.* **2010,** *1,* 2671-2674.
26. Kim, J.; Kim, B.-K.; Cho, S. K.; Bard, A. J. Tunneling Ultramicroelectrode: Nanoelectrodes and Nanoparticle Collisions. *J. Am. Chem. Soc.* **2014,** *136,* 8173-8176.
27. Castañeda, A. D.; Alligrant, T. M.; Loussaert, J. A.; Crooks, R. M. Electrocatalytic Amplification of Nanoparticle Collisions at Electrodes Modified with Polyelectrolyte Multilayer Films. *Langmuir* **2015,** *31,* 876–885.
28. Hill, C. M.; Kim, J.; Bard, A. J. Electrochemistry at a Metal Nanoparticle on a Tunneling Film: A Steady-State Model of Current Densities at a Tunneling Ultramicroelectrode. *J. Am. Chem. Soc.* **2015,** *137,* 11321-11326.
29. Kleijn, S. E. F.; Lai, S. C. S.; Miller, T. S.; Yanson, A. I.; Koper, M. T. M.; Unwin, P. R. Landing and Catalytic Characterization of Individual Nanoparticles on Electrode Surfaces. *J. Am. Chem. Soc.* **2012,** *134,* 18558-18561.
30. O'Connell, M. A.; Snowden, M. E.; McKelvey, K.; Gayet, F.; Shirley, I.; Haddleton, D. M.; Unwin, P. R. Positionable Vertical Microfluidic Cell Based on Electromigration in a Theta Pipet. *Langmuir* **2014,** *30,* 10011-10018.
31. Ebejer, N.; Schnippering, M.; Colburn, A. W.; Edwards, M. A.; Unwin, P. R. Localized High Resolution Electrochemistry and Multifunctional Imaging: Scanning Electrochemical Cell Microscopy. *Anal. Chem.* **2010,** *82,* 9141-9145.
32. Snowden, M. E.; Güell, A. G.; Lai, S. C. S.; McKelvey, K.; Ebejer, N.; O'Connell, M. A.; Colburn, A. W.; Unwin, P. R. Scanning Electrochemical Cell Microscopy: Theory and Experiment for Quantitative High Resolution Spatially-Resolved Voltammetry and Simultaneous Ion-Conductance Measurements. *Anal. Chem.* **2012,** *84,* 2483-2491.
33. Zhang, H.; He, H.-X.; Wang, J.; Liu, Z.-F. Atomic Force Microscopy Evidence of Citrate Displacement by 4-Mercaptopyridine on Gold in Aqueous Solution. *Langmuir* **2000,** *16,* 4554-4557.
34. Diao, P.; Jiang, D.; Cui, X.; Gu, D.; Tong, R.; Zhong, B. Studies of structural disorder of self-assembled thiol monolayers on gold by cyclic voltammetry and ac impedance. *J. Electroanal. Chem.* **1999,** *464,* 61-67.
35. Takehara, K.; Takemura, H.; Ide, Y. Electrochemical studies of the terminally substituted alkanethiol monolayers formed on a gold electrode: Effects of the terminal group on the redox responses of Fe(CN)3−6, Ru(NH3)3+6 and ferrocenedimethanol. *Electrochim. Acta* **1994,** *39,* 817-822.
36. Dasari, R.; Walther, B.; Robinson, D. A.; Stevenson, K. J. Influence of the Redox Indicator Reaction on Single-Nanoparticle Collisions at Mercury- and Bismuth-Modified Pt Ultramicroelectrodes. *Langmuir* **2013,** *29,* 15100-15106.
37. Kwon, S. J.; Fan, F.-R. F.; Bard, A. J. Observing Iridium Oxide (IrOx) Single Nanoparticle Collisions

at Ultramicroelectrodes. *J. Am. Chem. Soc.* **2010,** *132,* 13165-13167.
38. Zhou, Y. G.; Rees, N. V.; Compton, R. G. The Electrochemical Detection and Characterization of Silver Nanoparticles in Aqueous Solution. *Angew. Chem., Int. Ed.* **2011,** *50,* 4219-4221.
39. Zhao, J.; Wasem, M.; Bradbury, C. R.; Fermín, D. J. Charge Transfer across Self-Assembled Nanoscale Metal−Insulator−Metal Heterostructures. *J. Phys. Chem. C* **2008,** *112,* 7284-7289.
40. Bradbury, C. R.; Zhao, J.; Fermín, D. J. Distance-Independent Charge-Transfer Resistance at Gold Electrodes Modified by Thiol Monolayers and Metal Nanoparticles. *J. Phys. Chem. C* **2008,** *112,* 10153-10160.
41. Kang, M.; Perry, D.; Kim, Y.-R.; Colburn, A. W.; Lazenby, R. A.; Unwin, P. R. Time-Resolved Detection and Analysis of Single Nanoparticle Electrocatalytic Impacts. *J. Am. Chem. Soc.* **2015,** *137,* 10902-10905.
42. Kwon, S. J.; Zhou, H.; Fan, F.-R. F.; Vorobyev, V.; Zhang, B.; Bard, A. J. Stochastic electrochemistry with electrocatalytic nanoparticles at inert ultramicroelectrodes-theory and experiments. *PCCP* **2011,** *13,* 5394-5402.
43. Konopka, S. J.; McDuffie, B. Diffusion coefficients of ferri- and ferrocyanide ions in aqueous media, using twin-electrode thin-layer electrochemistry. *Anal. Chem.* **1970,** *42,* 1741-1746.
44. Singh, P. S.; Kätelhön, E.; Mathwig, K.; Wolfrum, B.; Lemay, S. G. Stochasticity in Single-Molecule Nanoelectrochemistry: Origins, Consequences, and Solutions. *ACS Nano* **2012,** *6,* 9662-9671.
45. Scanlon, M. D.; Peljo, P.; Mendez, M. A.; Smirnov, E.; Girault, H. H. Charging and discharging at the nanoscale: Fermi level equilibration of metallic nanoparticles. *Chem. Sci.* **2015,** *6,* 2705-2720.
46. Schweiss, R.; Welzel, P. B.; Werner, C.; Knoll, W. Dissociation of Surface Functional Groups and Preferential Adsorption of Ions on Self-Assembled Monolayers Assessed by Streaming Potential and Streaming Current Measurements. *Langmuir* **2001,** *17,* 4304-4311.
47. Hu, K.; Bard, A. J. Use of Atomic Force Microscopy for the Study of Surface Acid−Base Properties of Carboxylic Acid-Terminated Self-Assembled Monolayers. *Langmuir* **1997,** *13,* 5114-5119.
48. Krysiński, P.; Brzostowska-Smolska, M. Three-probe voltammetric characterisation of octadecanethiol self-assembled monolayer integrity on gold electrodes. *J. Electroanal. Chem.* **1997,** *424,* 61-67.
49. Angell, D. H.; Dickinson, T. The kinetics of the ferrous/ferric and ferro/ferricyanide reactions at platinum and gold electrodes: Part I. Kinetics at bare-metal surfaces. *J. Electroanal. Chem. Interfacial Electrochem.* **1972,** *35,* 55-72.
50. Chen, S.; Liu, Y.; Chen, J. Heterogeneous electron transfer at nanoscopic electrodes: importance of electronic structures and electric double layers. *Chem. Soc. Rev.* **2014,** *43,* 5372-5386.
51. Morris, R. B.; Franta, D. J.; White, H. S. Electrochemistry at platinum bane electrodes of width approaching molecular dimensions: breakdown of transport equations at very small electrodes. *The Journal of Physical Chemistry* **1987,** *91,* 3559-3564.
52. Smith, C. P.; White, H. S. Theory of the voltammetric response of electrodes of submicron dimensions. Violation of electroneutrality in the presence of excess supporting electrolyte. *Anal. Chem.* **1993,** *65,* 3343-3353.
53. Seibold, J. D.; Scott, E. R.; White, H. S. Diffusional transport to nanoscopic band electrodes. *J. Electroanal. Chem. Interfacial Electrochem.* **1989,** *264,* 281-289.
54. Watkins, J. J.; Zhang, B.; White, H. S. Electrochemistry at Nanometer-Scaled Electrodes. *J. Chem. Educ.* **2005,** *82,* 712.
55. He, R.; Chen, S.; Yang, F.; Wu, B. Dynamic Diffuse Double-Layer Model for the Electrochemistry of Nanometer-Sized Electrodes. *J. Phys. Chem. B* **2006,** *110,* 3262-3270.
56. Xiaoling, Y.; Guigen, Z. Simulating the structure and effect of the electrical double layer at nanometre electrodes. *Nanotechnology* **2007,** *18,* 335201.
57. Ball, P. Chemical physics: How to keep dry in water. *Nature* **2003,** *423,* 25-26.
58. Noy, A.; Vezenov, D. V.; Lieber, C. M. Chemical force microscopy. *Annu. Rev. Mater. Sci.* **1997,** *27,* 381-421.
59. Butt, H.-J.; Cappella, B.; Kappl, M. Force measurements with the atomic force microscope: Technique, interpretation and applications. *Surf. Sci. Rep.* **2005,** *59,* 1-152.
60. Kakiuchi, T.; Iida, M.; Imabayashi, S.-i.; Niki, K. Double-Layer-Capacitance Titration of Self-Assembled Monolayers of ω-Functionalized Alkanethiols on Au(111) Surface. *Langmuir* **2000,** *16,* 5397-5401.
61. Fawcett, W. R.; Fedurco, M.; Kovacova, Z. Double Layer Effects at Molecular Films Containing Acid/Base Groups. *Langmuir* **1994,** *10,* 2403-2408.
62. White, H. S.; Peterson, J. D.; Cui, Q.; Stevenson, K. J. Voltammetric Measurement of Interfacial Acid/Base Reactions. *J. Phys. Chem. B* **1998,** *102,* 2930-2934.
63. Bard, A. J.; Faulkner, L. R. *Electrochemical Methods: Fundamentals and Applications*; Wiley2000.
64. Mazurenka, M.; Hamilton, S. M.; Unwin, P. R.; Mackenzie, S. R. In-Situ Measurement of Colloidal Gold Adsorption on Functionalized Silica Surfaces. *J. Phys. Chem. C* **2008,** *112,* 6462-6468.
65. Burgess, I.; Seivewright, B.; Lennox, R. B. Electric Field Driven Protonation/Deprotonation of Self-

Assembled Monolayers of Acid-Terminated Thiols. *Langmuir* **2006,** *22,* 4420-4428.
66. Sánchez, S.; Soler, L.; Katuri, J. Chemically Powered Micro- and Nanomotors. *Angew. Chem. Int. Ed.* **2015,** *54,* 1414-1444.
67. Eriksson, J. C.; Ljunggren, S.; Claesson, P. M. A phenomenological theory of long-range hydrophobic attraction forces based on a square-gradient variational approach. *J. Chem. Soc., Faraday Trans. 2* **1989,** *85,* 163-176.
68. Wood, J.; Sharma, R. How Long Is the Long-Range Hydrophobic Attraction? *Langmuir* **1995,** *11,* 4797-4802.
69. Ederth, T.; Liedberg, B. Influence of Wetting Properties on the Long-Range "Hydrophobic" Interaction between Self-Assembled Alkylthiolate Monolayers. *Langmuir* **2000,** *16,* 2177-2184.
70. Ishida, N.; Inoue, T.; Miyahara, M.; Higashitani, K. Nano Bubbles on a Hydrophobic Surface in Water Observed by Tapping-Mode Atomic Force Microscopy. *Langmuir* **2000,** *16,* 6377-6380.
71. Tyrrell, J. W. G.; Attard, P. Images of Nanobubbles on Hydrophobic Surfaces and Their Interactions. *Phys. Rev. Lett.* **2001,** *87*, 176104.
72. Attard, P. Thermodynamic Analysis of Bridging Bubbles and a Quantitative Comparison with the Measured Hydrophobic Attraction. *Langmuir* **2000,** *16,* 4455-4466.